Local structure and magnetic behaviour of Fe-doped TiO_2 anatase nanoparticles: experiments and calculations

J. Phys.: Condens. Matter **20** (2008) 135210 (9pp) doi:10.1088/0953-8984/20/13/135210

Local structure and magnetic behaviour of Fe-doped TiO_2 anatase nanoparticles: experiments and calculations

C E Rodríguez-Torres[1], A F Cabrera[1], L A Errico[1], C Adán[2], F G Requejo[1,3], M Weissmann[4] and S J Stewart[1]

[1] IFLP-CONICET and Departamento de Física, Facultad de Ciencias Exactas, Universidad Nacional de La Plata, CC 67, 1900 La Plata, Argentina
[2] Instituto de Catálisis y Petroleoquímica, CSIC 49706 Cantoblanco, Madrid, Spain
[3] INIFTA, Facultad de Ciencias Exactas, Universidad Nacional de La Plata, CC 16 sucursal 4, 1900 La Plata, Argentina
[4] Departamento de Física, Comisión Nacional de Energía Atómica, Avenida del Libertador 8250, 1429 Buenos Aires, Argentina

E-mail: stewart@fisica.unlp.edu.ar

Received 1 January 2008
Published 7 March 2008
Online at stacks.iop.org/JPhysCM/20/135210

Abstract

We present an investigation of Fe-doped TiO_2 anatase nanoparticles (2.8 and 5.4 at.% Fe) where Fe substitutes Ti atoms without the presence of other phases. In order to characterize these samples we used x-ray absorption experiments, ^{57}Fe Mössbauer spectroscopy, *ab initio* calculations and magnetometry. Results from iron K-edge near-edge and extended x-ray absorption fine structure confirm that Fe^{3+} replaces Ti^{4+} in the TiO_2 anatase structure increasing the metal-anion bond length. Mössbauer spectra recorded at room temperature show asymmetric Fe^{3+} broad doublets. These results agree with structural, hyperfine and magnetic properties calculated using density-functional theory, if oxygen vacancies are present in the iron–oxygen octahedra. Mössbauer and magnetic measurements indicate that samples are paramagnetic at room temperature. At low temperatures, two kind of magnetic species can be distinguished: (i) isolated paramagnetic Fe^{3+} ions and (ii) antiferromagnetically coupled Fe^{3+} ions. These results also show that substitutional Fe in nanosized anatase TiO_2 does not induce ferromagnetic ordering.

1. Introduction

Doped anatase-type TiO_2 is a widely studied photocatalyst semiconductor [1–3]. Iron (III) doping of nanosized TiO_2 has been demonstrated to enhance its photoactivity efficiency [4–6] although its role concerning the hole–electron recombination process is still unclear [7]. Several synthesis methods have been employed to reach an optimum solubility of Fe in anatase and avoid the segregation of Fe–Ti–O or Fe–O impurity phases that reduce its photoactivity. However, when the level of doping is low the clear identification of whether Fe ions occupy substitutional or interstitial sites in the TiO_2 lattice or form spurious phases can be difficult to ascertain [8, 9]. Therefore, the use of a variety of techniques is crucial to obtain a precise picture about this diluted system and properly interpret its physico-chemical properties.

Fe-doped TiO_2 is also of significant interest in magnetism. Indeed, systems formed by the presence of magnetic ions in non-magnetic matrices (diluted magnetic semiconductors (DMS) or diluted magnetic insulators (DMI)) have attracted considerable interest in recent years due to their potential application in spintronic and magneto-optic devices [10]. However, contradictory experimental as well as theoretical results were obtained [11–22], and it is uncertain whether the ferromagnetic signal (FM) found in some cases is intrinsic or comes from extrinsic magnetic phases. Conjectures were usually based on macroscopic experimental results but relatively little attention was given to the local structure around the dopants. Knowledge of the local environment of the dopant is essential to understand the mechanisms giving rise to magnetic order in these compounds [20]. In particular, as the FM signals with Curie temperatures above room temperature

were mainly detected in thin film systems (e.g. Fe-or Co-doped TiO_2 [12–14, 16]), it seems that spatial dimensionality might play an important role. It is therefore interesting to investigate how the reduction of the structural correlation length down to the nanoscale range might influence the magnetic behaviour.

To this aim, we present here an investigation on Fe-doped anatase TiO_2 nanoparticles of about 10–13 nm, which were prepared by a microemulsion method. By combining Mössbauer and x-ray absorption spectroscopies with *ab initio* calculations, we are able to give an exhaustive characterization of the local structure around Fe in TiO_2 anatase nanoparticles. These results also demonstrate that Fe substitutes Ti in the anatase structure and no other spurious phases are present. The magnetic properties of these impurity-free $Fe_xTi_{1-x}O_2$ samples were investigated, using ac-susceptibility and dc-magnetization measurements.

2. Experimental details

Fe-doped TiO_2 anatase-type nanoparticles of composition 2.8 and 5.4 at.% Fe (hereafter labelled SA and SB, respectively) were synthesized by a microemulsion method. Details of sample preparation were published elsewhere [4]. The atomic percentages were determined by inductively coupled plasma atomic emission spectroscopy. X-ray diffraction data (not shown here) showed that all samples are single-phase with the anatase structure. The average grain size estimated by Scherrer's equation is about 10 and 13 nm for SA and SB, respectively.

Room temperature XANES and EXAFS spectra at the Fe K-edge (7112 eV) and Ti K-edge (4966 eV) were recorded in transmission mode using a Si(111) monochromator at the XAS beamline of the LNLS (Laboratorio Nacional de Luz Sincrotron) in Campinas, Brazil. The spectra analysis was performed by pre-edge background subtraction followed by a normalization procedure considering the extended region. The fine structure oscillations $\chi(k)$ of each spectrum in the extended region were isolated using the ATHENA program [23] and Fourier transformed over a specific k range.

^{57}Fe Mössbauer spectra in the 23–300 K range of temperature were taken in transmission geometry with a nominal 20 mCi ^{57}Co source in the Rh matrix with a linear velocity waveform and using a Displex closed cycle cryostat. The 4.2 K spectra were taken in a cryostat with both source and sample at liquid helium temperature and a sinusoidal velocity waveform. Isomer shifts (IS) are referred to metallic α-Fe at room temperature.

The thermal dependence of the in-phase and out-of-phase components of the ac-susceptibility was measured in a LakeShore 7130 ac susceptometer. The alternating field was of 0.1 mT at a frequency of 825 Hz. dc-magnetic measurements were performed using a Superconductor Quantum Interference Device MPMS from Quantum Design.

3. Calculation details

We performed *ab initio* electronic structure calculations to determine the self-consistent potential and the charge density inside the anatase TiO_2 cell. Our aim here is to obtain from first-principles calculations hyperfine parameters at an Fe impurity replacing Ti in anatase, taking properly into account the structural and electronic effects introduced by the impurity (and oxygen vacancies) in the host lattice. We simulate this non-periodic system considering a periodically repeated large unit cell where a single Fe atom replaces a single Ti in the anatase TiO_2 host. We consider a periodic three-dimensional system, as the studied nanoparticles contain many unit cells of anatase. From these first-principles calculations we obtained the isomer shift (IS) and quadrupole splitting (QS) hyperfine parameters corresponding to the iron nucleus in the anatase lattice. The IS is given by [24]:

$$\mathrm{IS} = \alpha(\rho_a(0) - \rho_b(0)) \tag{1}$$

where $\rho_a(0)$ and $\rho_b(0)$ are the electron charge density at the nuclear site for the absorber (a) and the source (b), respectively. α is a calibration constant of about $-0.21a_o^{-3}$ mm s^{-1} (a_o is the Bohr ratio) [25]. By performing IS shift calculations on well known Fe compounds such as γ-Fe, FeO and Fe_2O_3, using the same code and precision as in the present work, we found that for our calculations $\alpha = -0.23a_o^{-3}$ mm s^{-1}. The QS is given by [24]:

$$\mathrm{QS} = \frac{eQ_\mathrm{N}}{2} V_{zz} \left(1 + \frac{\eta^2}{3}\right)^{1/2} \tag{2}$$

where Q_N is the nuclear-quadrupole moment of the 14 keV excited state of ^{57}Fe ($Q_\mathrm{N} = 0.16b$) [26], V_{zz} is the principal component of the electric field gradient (EFG) and η the asymmetry parameter [24].

The unit cell of TiO_2 with anatase structure (tetragonal, space group $I4_1/amd$, $a = b = 3.782$ Å, $c = 9.502$ Å) contains four Ti atoms at positions [(0, 0, 0); (0, 1/2, 1/4); BC] and eight O at positions [(0, 0, u); (0, 0, $-u$); (0, 1/2, $u+$ 1/4); (0, 1/2, 1/4 $-$ u); BC] with $u = 0.2066$ (BC body centred) [26, 27]. Each Ti atom is surrounded by a slightly distorted octahedron TiO_6 (figure 1) with a rectangular basal plane of oxygen atoms (O1) with distances to Ti (1.93 Å) slightly shorter than those of the other two atoms at apical positions (O2) (1.98 Å). The supercell (SC) considered here consists of four unit cells of anatase TiO_2 with one Ti atom replaced by the Fe impurity atom. This gives a composition $Ti_{0.9375}Fe_{0.0625}O_2$, which represents about 6 at.% of doping. The resulting 48-atoms SC has dimensions $a' = 2a = b' = 2b = 7.564$ Å, $c' = c = 9.502$ Å. We have performed calculations assuming different scenarios. Firstly, we analyse the effect of Fe-substitution. Secondly, we consider the effect of both substitutional iron at metal sites and the formation of oxygen vacancies. In our calculations, the oxygen vacancy is created simply by taking out one oxygen atom from the supercell. In the latter, we have analysed three situations: (i) by removing a basal oxygen atom (O1 in figure 1) from Fe-containing octahedron (FeO_6), (ii) by removing a vertex oxygen (O2 in figure 1) from FeO_6 and (iii) from the Ti-containing octahedron (O3 in figure 1).

We employed the *ab initio* full-potential linearized-augmented plane waves (FPLAPW) method [28, 29] to solve

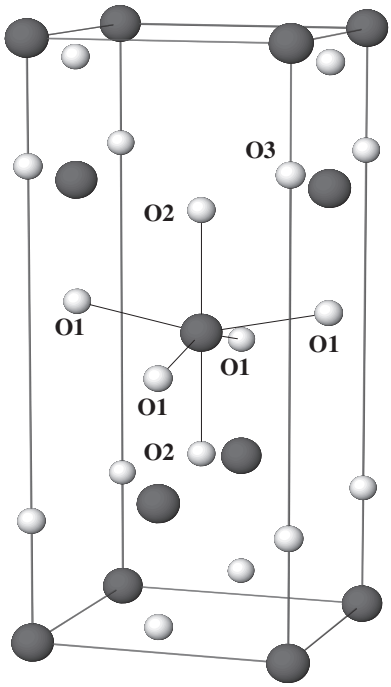

Figure 1. Anatase TiO_2 unit cell. Black and white spheres represent Ti and O, respectively. O1 indicates basal positions and O2 apical positions of oxygen nearest neighbours (O_{NN}), while O3 indicates oxygen next nearest neighbours (O_{NNN}) of metal sites in anatase.

the Kohn–Sham equations in the framework of the density-functional theory (DFT). Spin-polarized electronic structure calculations were performed with the WIEN2K code [30] in a scalar relativistic version without spin–orbit coupling. Exchange and correlation effects were treated within density-functional theory using the LSDA approximation [31]. In the FPLAPW method no shape approximation on either the potential or the electronic charge-density is made, being thus specially suited for EFG calculations. For methodological purposes the unit cell is divided into non-overlapping spheres with radius R_i and an interstitial region. The atomic spheres radii used for Fe, Ti and O were 1.00, 0.95 and 0.80 Å, respectively. The parameter RK_{max}, which controls the size of the basis set, was set to 6.0 (R is the smallest muffin tin radius and K_{max} the largest wavenumber of the basis set). We also introduced local orbitals to include Ti-3s and 3p, O-2s and Fe-3p levels. Integration in the reciprocal space was performed using the tetrahedron method taking 100 k-points in the first Brillouin zone. Once self-consistency of the potential was achieved, quantum-mechanically-derived forces were obtained and the ions were displaced according to a Newton-damped scheme, and then the new positions for the atoms were obtained (for details, see [32]). The procedure was repeated until the forces on the ions were below a tolerance value taken as 0.01 eV $Å^{-1}$. At each position the V_{ii} elements of the EFG tensor were obtained directly from the V_{2M} components of the lattice harmonic-expansion of the self-consistent potential [33].

The precision of the present FPLAPW calculations is given by the size of the basis set and the k-mesh sampling. To check the accuracy of the present results we performed several additional calculations. For selected systems, we increased the basis set (number of plane waves) from $RK_{max} = 5.0$ to $RK_{max} = 7.0$. We also increased the number of k-points from 50 to 150. We also studied the effect of the muffin-tin radii on the relevant electronic and structural properties of the system. Magnetic moments, electric field gradients, IS and interatomic distances can be obtained with adequate precision using $RK_{max} = 6.0$ and 100 k-points (the interatomic distances, EFG components and IS are converged in less than 0.01 Å, 0.1×10^{21} V m^{-2} and 0.03 mm s^{-1}, respectively). Structural relaxation, leading to forces on the atoms less than 0.01 eV $Å^{-1}$, is the most important factor for convergence of the electronic properties, and they do not change by increasing the number of plane waves or of k-points. This is not the same for the total energy that requires a larger number of plane waves and of k-points for convergence. However, the energy differences are well converged for the employed parameters.

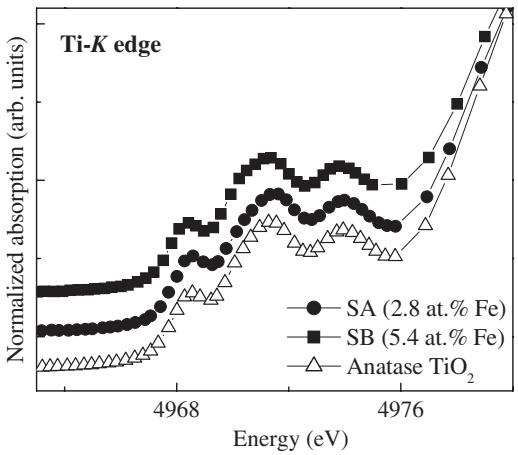

Figure 2. Pre-edge region of XANES spectra at the Ti K-edge of SA ($x = 2.8$ at.% Fe), SB ($x = 5.4$ at.% Fe). Spectrum of bulk TiO_2 anatase is also shown for comparison.

4. Results

4.1. Ti and Fe K-edge XANES results

The pre-edge Ti K-edge XANES structure arises from a $1s \rightarrow 3d$ dipole electronic transition, being the peak intensities affected by the local geometry and the particular medium-range structure of the sample around central Ti atoms [34, 35]. Figure 2 shows the comparison between normalized Ti-K XANES spectra at the pre-edge region of bulk anatase (a-TiO_2) and Fe-doped TiO_2 nanoparticles. From here we clearly observe that these spectra confirm the anatase-type structure of SA and SB, in agreement with the x-ray diffraction results. Moreover, pre-edge features (figure 2), i.e. the height and position of the pre-peaks, reveal that these samples only contain hexa-coordinated Ti atoms [35]. Additionally, from the Ti-K XANES results we do not detect the presence of Ti^{3+}. Due to the relatively low iron content, no appreciable changes inherent to doping are expected to affect the Ti K-edge energy region.

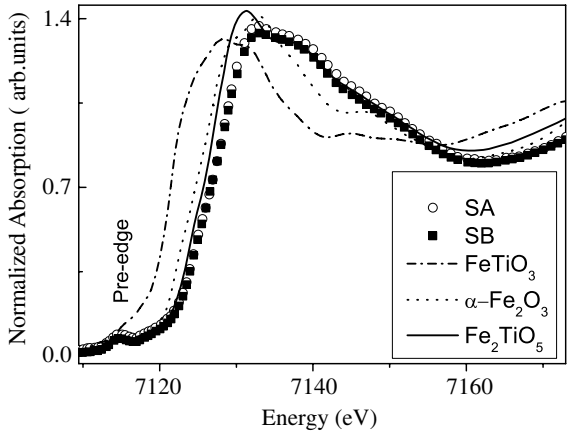

Figure 3. XANES spectra at the Fe K-edge of Fe-doped TiO_2 samples, SA and SB. Spectra of bulk hematite α-Fe_2O_3, ilmenite $FeTiO_3$ and pseudobrookite Fe_2TiO_5 are also shown for comparison.

Figure 3 shows the Fe-K XANES spectra of Fe-doped TiO_2. In addition, the spectra of ilmenite $FeTiO_3$, hematite α-Fe_2O_3 and pseudobrookite Fe_2TiO_5 are shown for comparison. In these cases, the pre-edge structure arises from electronic 1s $\rightarrow$ 3d quadrupole and 1s $\rightarrow$ 3d/4p dipole electronic transitions [36]. We observe that a pre-edge feature is present in both Fe-doped TiO_2 samples and its intensity reflects Fe-sites with O_h symmetry. XANES spectra have similar edge energies regardless of Fe content and they are compatible with Fe ions with +3 oxidation state [37]. The Fe absorption edges are shifted ~2.1 and 2.8 eV upward with respect to α-Fe_2O_3 and $FeTiO_3$ spectra respectively, while Fe_2TiO_5 is within the resolution (~0.5 eV). After the absorption edge, the same features are observed for both Fe-doped samples but they clearly differ from those corresponding to $FeTiO_3$, α-Fe_2O_3 or Fe_3O_4 (not shown). Although more similarities are observed when compared to Fe_2TiO_5 electronic features, the main-edge crest at 7132 eV (1s $\rightarrow$ 4p transition) is less resolved and the peaks are broader, indicating a distinct Fe environment. Further, the peak broadening is probably related to iron distribution among locally disordered sites whose energy transition varies according to the average bond length.

Table 1. Fe K-edge EXAFS simulation results obtained by assuming Fe substitutionally placed at TiO_2 anatase metal sites. N is the average coordination number, R the distance from the central atom, E_0 the correction to the threshold energy and σ^2 the Debye–Waller factor.

	Atom type	N	R (Å)	σ^2 (Å^2)	E_0 (eV)
	O	4	1.93	0.0070	−5
Fe in TiO_2	O	2	1.964	0.0070	−5
anatase	Ti	4	3.04	0.0135	−5
(Fe K-edge)	Ti	4	3.785	0.0135	−5
	MS[a]	8	3.83	0.0270	−5
	O	8	3.87	0.0270	−5

[a] MS refers to multiple scattering paths of multiplicity 2.

4.2. Fe K-edge EXAFS results

The local environment of Fe in $Fe_xTi_{1-x}O_2$ samples was also examined by inspecting the Fe K-edge EXAFS region. Figure 4 shows the EXAFS oscillations (a) and the corresponding Fourier transform (FT) (b). We observe that the oscillations of SA and SB are similar to each other (figure 4(a)) but quite different to those expected for the most common Fe–Ti oxides (Fe_2TiO_5, $FeTiO_3$) or Fe oxides (not shown here). On the other hand, we observe that the FTs are comparable to the Ti K-edge FT corresponding to anatase TiO_2 (see figure 4(c)).

To compare these results with a theoretical standard we have performed an EXAFS simulation using FEFF7 code [38]. We considered single and multi-scattering paths corresponding to the five successive atomic shells around Fe substitutionally placed at Ti-sites in anatase-TiO_2. Figure 4 shows the good agreement between experimental and simulated results obtained using the parameters shown in table 1. From this analysis we can infer that Fe ions are diluted in TiO_2 occupying Ti-sites of the anatase structure.

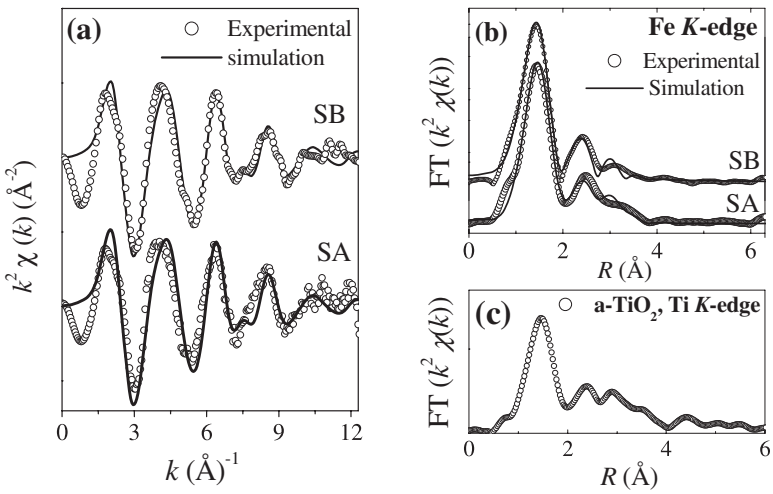

Figure 4. The $k^2\chi(k)$ functions (a) and the corresponding Fourier transforms (FT) (b) of samples SA and SB (Fe K-edge). The FT for TiO_2 anatase (Ti K-edge) is also shown for comparison (c). Solid lines represent the simulations using the parameters shown in table 1.

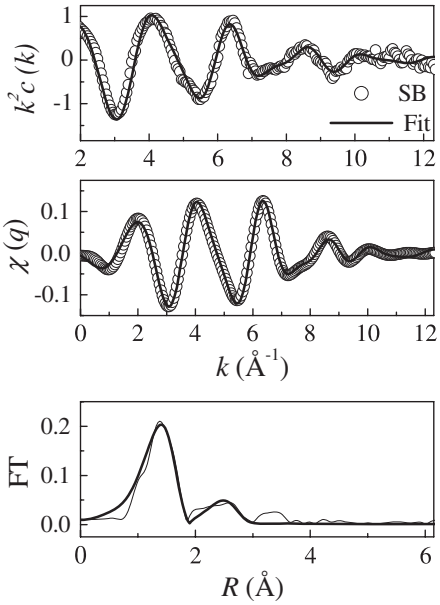

Figure 5. The $k^2\chi(k)$ function, the back-transformed FT (R between 0.56 and 2.91 Å) and the Fourier transform (FT) of sample SB (open circles) and the corresponding fits (bold lines).

Table 2. Ti and Fe K-edge EXAFS fitted parameters. F means that the parameter was kept fixed along the fitting. S_0^2 is the scattering amplitude.

$S_0^2 = 0.75$	Atom type	N	R (Å)	σ^2 (Å^2)	E_0 (eV)
Anatase	O	6 (F)	1.94_1	0.0049_8	-6_1
(Ti K-edge)	Ti	4 (F)	3.04_3	0.0082_8	-6_1
SA	O	5.5_7	1.97_2	0.007_2	-5_2
(Fe K-edge)	Ti	$3.9_{1.5}$	3.01_6	0.022_7	-5_2
SB	O	5.7_5	1.960_7	0.007_4	-5_1
(Fe K-edge)	Ti	2.8_7	3.01_4	0.010_{82}	-5_1
Anatase	O	6	1.946		
(theoretical)	Ti	4	3.04		

To further analyse the effect of Fe-doping on the local structure of metal sites in anatase, the first and second peaks of the FT (figure 4(b)) were back-transformed and fitted by considering two atomic shells. The first shell corresponds to oxygen nearest neighbours O_{NN}, and the second one to titanium second neighbours of Fe-sites in anatase (see table 2). Figure 5 shows the good agreement between fit and experimental data for SB. Similar results were obtained for SA. Although EXAFS fitting results show effective Fe coordination numbers lower than six (table 2), the estimated errors in their determination (∼12%) cannot allow a clear detection of anionic vacancies probably created to maintain the local charge neutrality. We observe that the presence of Fe in the TiO_2 lattice causes an augmentation of cation–oxygen bond lengths with respect to Ti–O distances in a-TiO_2 (see table 2). A recent investigation performed by Zhu *et al* [39] reports similar results for anatase nanoparticles prepared by the sol–gel method when doped with 1 wt% of Fe (approx. 1.5 at.%). For higher Fe contents, their EXAFS results clearly show the presence of α-Fe_2O_3, a fact that is not observed in our case.

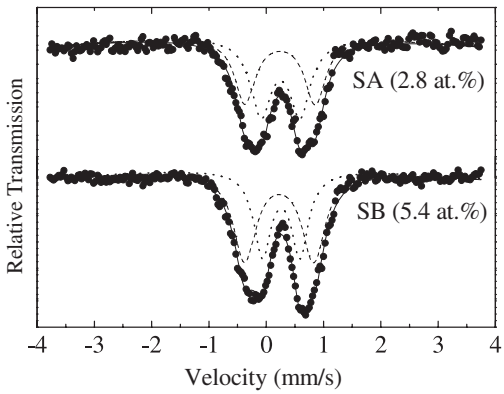

Figure 6. Room temperature Mössbauer spectra and fitting curves for Fe-doped TiO_2 samples.

4.3. Mössbauer investigation

Room temperature Mössbauer spectra of Fe-doped anatase TiO_2 only show broad asymmetric non-magnetic signals belonging to Fe^{3+} (figure 6). Spectra taken in a higher velocity range scale (not shown here) did not display resolved magnetic components. The doublets were best fitted with two quadrupolar interactions, I and II (table 3). We observe that the QS_I relative area slightly increases with the iron concentration at the expense of the QS_{II} doublet (table 3). Previous Mössbauer studies on Fe-doped TiO_2 anatase have also reported the presence of non-magnetic components at room temperature but with varied QS values. For instance, Cordishi *et al* [8] assigned a doublet with QS = 1.24 mm s^{-1} to Fe $^{3+}$ ions in solid solution in the anatase phase, while Hirano *et al* [9] reported a QS = 0.6 mm s^{-1} value for Fe^{3+} in the same phase. Recently, Zhu *et al* [21] reported a doublet with QS = 1.13 mm s^{-1} for Fe^{3+} substitutional in anatase TiO_2 nanocomposites plus a secondary doublet (QS = 0.71 mm s^{-1}) that they assigned to superparamagnetic (SPM) hematite α-Fe_2O_3. In that case, the percentage of hematite (in both SPM and blocked states) was found to increase with the iron doping. In our case, although QS_I and QS_{II} are within the 0.50–1.20 mm s^{-1} range usually reported for SPM α-Fe_2O_3 [40], its presence can be ruled out since no evidence of any blocking of α-Fe_2O_3 particle magnetic moments was observed either in the magnetic measurements or in the thermal evolution of the Mössbauer spectra (see discussion below).

At $T = 4.2$ K the resonant lines broaden and relaxation effects dominate the Mössbauer lineshape (figure 7). To take into consideration these relaxation effects we have included a broad single central line in our fitting procedure. The SB spectrum shows also the emergence of a broad sextet, which was fitted assuming a distribution of magnetic sites. The average hyperfine field of $B_{hf} = 40$ T indicates that the sextet belongs to Fe^{3+} in an oxide phase. Mössbauer spectra recorded at temperatures within the 23–200 K range (not shown here) only showed non-magnetic components. Conversely, the SA spectrum does not show resolved magnetic contributions down to 4.2 K but a relaxation broadening. From the fitting we found that the non-magnetic and non-relaxing components, i.e. the paramagnetic components even present at 4.2 K, roughly

Table 3. Room temperature hyperfine parameters: QS is the quadrupole splitting, IS is the isomer shift, Γ is the linewidth, A is the relative area. Subscripts I and II refer to two different iron sites. J is the total angular moment derived from fitting M–H curves using equation (1) and μ_{eff} is the effective magnetic moment.

	QS_I (mm s^{-1})	IS_I (mm s^{-1})	Γ_I (mm s^{-1})	A_I (%)	QS_{II} (mm s^{-1})	IS_{II} (mm s^{-1})	Γ_{II} (mm s^{-1})	A_{II} (%)	J	μ_{eff} (μ_B/Fe)
2.8 at.% (SA)	1.23_3	0.35_1	0.44_4	47_8	0.68_3	0.36_1	0.44_3	53_8	1.88_5	4.7_1
5.4 at.% (SB)	1.20_2	0.330_4	0.49_2	59_4	0.66_1	0.366_4	0.36_2	41_4	1.80_5	4.5_1

Table 4. Largest component, V_{zz}, and asymmetry parameter, η, of the electric field gradient EFG tensor at the Fe site in anatase TiO_2 obtained in the FPLAPW calculations. d (Fe–O_{NN}) are the distances from Fe to its oxygen nearest neighbours O_{NN}. The number in brackets indicates the multiplicity. d^{aver} is the mean Fe–O_{NN} bond length. Isomer shifts IS and quadrupole splitting QS were calculated from V_{zz} and η. To compare with the experimental results, the absolute value of QS must be considered.

Configuration	d (Fe–O_{NN}) (Å)	d (Fe–O_{NN}) (Å)	V_{zz} (10^{21} V m^{-2})	η	IS (mm s^{-1})	QS (mm s^{-1})
$Ti_{0.9375}Fe_{0.0625}O_2$	1.82 [2] 1.96 [4] d^{aver}: 1.91	d^{aver}: 3.04	+1.73	0.00	0.11	+0.29
$Ti_{0.9375}Fe_{0.0625}O_{1.97}$ vacancy at O1	1.94 [2] 1.95 1.99 2.01 d^{aver}: 1.966	d^{aver}: 3.03	−5.06	0.04	0.48	+0.95
$Ti_{0.9375}Fe_{0.0625}O_{1.97}$ vacancy at O2	1.92 [2] 1.95 [2] 2.10 d^{aver}: 1.968	d^{aver}: 3.03	−3.30	0.06	0.42	+0.55
$Ti_{0.9375}Fe_{0.0625}O_{1.97}$ vacancy at O3	1.96 1.98 [3] 2.06 [2] d^{aver}: 2.00	d^{aver}: 2.97	+5.40	0.56	0.53	−0.92

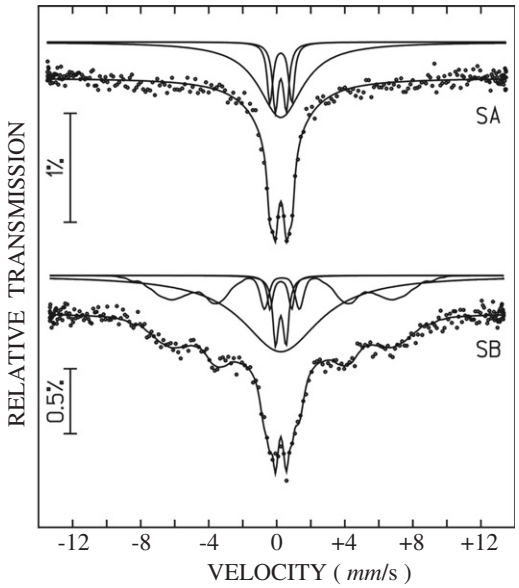

Figure 7. Mössbauer spectra recorded at 4.2 K for SA and SB.

represent 30 and 15% of the total resonant area for SA and SB, respectively.

4.4. Ab initio calculations

Our *ab initio* calculations showed that the presence of Fe impurities at metal sites in anatase TiO_2 host induces structural distortions that affect the Fe–O_{NN} nearest neighbour bond lengths. These distortions are anisotropic, i.e. Fe–O2 bond lengths (figure 1) shorten by about 0.16 Å while the Fe–O1 distances enhance by about 0.03 Å with respect to Ti–O_{NN} average distances in anatase (see table 4). Further, we have observed that after the structural relaxation process Fe–O1 distances become larger than Fe–O2 ones, contrary to the initial unrelaxed structure. These impurity-induced distortions differ from those nearly isotropic Fe–O_{NN} contractions found in Fe-doped rutile TiO_2 using this method of calculation [41].

The average Fe–O_{NN} relaxed bond lengths (1.91 Å) are in poor agreement with the EXAFS results (1.97 Å). Further, our FPLAPW calculations predict an IS of 0.11 mm s^{-1} (table 4), which is far from the experimental results. Neither does the QS value agree with the results obtained from the fitting (tables 3 and 4). Thus, we conclude that a simple substitutional doping model cannot account for our Mössbauer and EXAFS results and additional effects must be considered to correctly reproduce the present data.

In a second scenario we included the formation of oxygen vacancies along with substitutional Fe-doping. Our calculations showed that the vacancies cause a large structural relaxation, a fact to be expected due to the ionic character of TiO_2, and a symmetry breaking around Fe-sites (table 4). Anionic vacancies at Fe–O_{NN} octahedra (sites O1 or O2 in figure 1) were found to be energetically more favourable than vacancies at Fe–O_{NNN} next nearest neighbour locations (sites O3). Regarding the hyperfine parameters, a vacancy located at O1 or O2 produces an increment of the IS from 0.11 mm s^{-1}

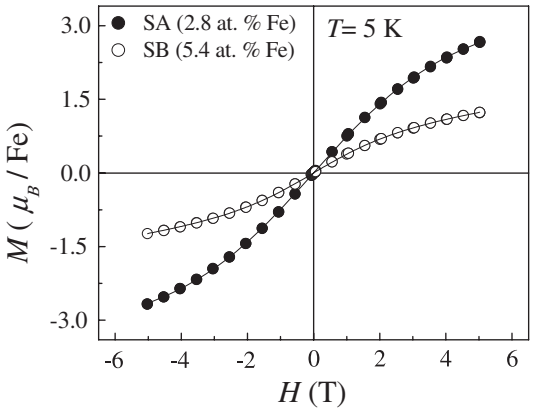

Figure 8. M–H curves taken at 5 K. Solid lines are the results of the fitting procedure as described in the text.

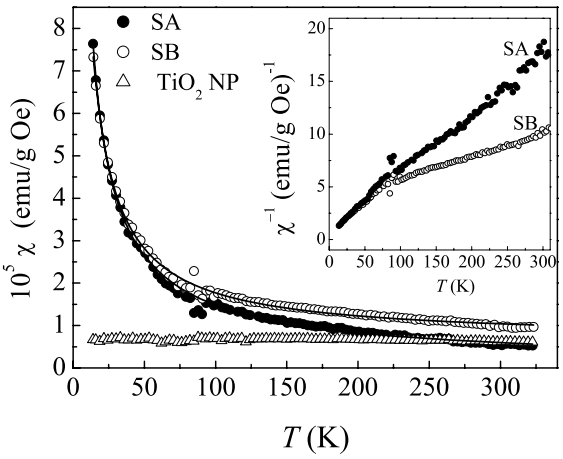

Figure 9. Thermal dependence of the inverse of the low field in-phase component of the ac-susceptibility (χ), for SA, SB. $\chi(T)$ of un-doped TiO_2 nanoparticles (NP) is also shown. Solid lines show fits to the modified Curie–Weiss function as described in the text. The dispersion of points in the 75–100 K region has an instrumental origin.

(without vacancies) up to 0.42 mm s^{-1} (table 4), in better accordance with our experimental results. Furthermore, for both configurations the average Fe–O_{NN} bond length is 1.97 Å (table 4), in very good agreement with the distances obtained from the EXAFS analysis (table 1). Moreover, FPLAPW also reproduces the experimentally found Fe–Ti_{NN} distances.

The QS ratio between sites with vacancies at the basal and apical positions agrees with the experimental ratio QS_I/QS_{II} of about 2. We therefore associate sites QS_I and QS_{II} with Fe located substitutionally and with oxygen vacancies nearby. However, other vacancy configurations could be present and they would contribute to broaden the Mössbauer resonant lines.

Concerning the magnetic part, the magnetic moment that results from our calculations gives 4.0 μ_B per supercell, and is almost independent of the induced local structural distortions. Further, spin-polarization occurs mainly at the impurity sites. When oxygen vacancies are not considered, the magnetic moment in the Fe muffin-tin spheres is 3.00 μ_B/Fe atom, and this value is enlarged to 3.5 μ_B/Fe atom after including vacancies. In addition, our calculations performed considering two Fe impurities per supercell predict that antiferromagnetic alignments are energetically more favourable than the ferromagnetic ones. This result coincides with that obtained for Fe-doped rutile TiO_2 [41]. It is worth considering that the overall properties of Fe-doped TiO_2 are probably the effect of an average of different impurity-defect configurations. Therefore, for a more realistic calculation, large supercells with more than two impurities and different numbers of oxygen vacancies would be necessary. However, this study is far more complicated since the concentration and distribution of impurities and vacancies are additional parameters.

4.5. Magnetic characterization

The magnetization (M–H) curves were recorded at 300 and 5 K. We observe that Fe-doped TiO_2 samples remain mainly paramagnetic down to the lowest temperature (see figure 8). We fitted the 5 K M–H curve by [42]

$$M = NgJ\mu_B B_J(x) \tag{3}$$

where $B_J(x)$ is the Brillouin function, $x = gJ\mu_B H/k_B T$, N is the number of magnetic entities per gram, g is the Landé-factor, μ_B the Bohr magneton, J is the total quantum number and k_B is the Boltzmann constant. This gives effective magnetic moments, $\mu_{eff} \sim 4.7$ and 4.5 μ_B for SA and SB, respectively (see table 3).

The 300 K M–H curves were fitted to the linear function $M = N'g^2J(J+1)\mu_B^2 H/3k_B T$ (i.e. the limit of equation (3) when $x \ll 1$). Using the J values obtained from the 5 K curves; we estimated the number of total paramagnetic ions at room temperature (N'). Comparing N' and N, we estimated that 56 and 32% of the total magnetic ions remain paramagnetic down to 5 K for samples SA and SB, respectively. This would imply that there is another fraction of Fe ions that establishes a local order since no evidence of a ferri-or ferromagnetic order is observed.

The low field in-phase ac-susceptibility (χ) of $Fe_xTi_{1-x}O_2$ samples monotonically decreases on raising the temperature (figure 9). Further, the reciprocal susceptibility χ^{-1} deviates from ~100 K of the linear behaviour shown at high temperatures (see inset figure 9), such deviation being more pronounced for SB. χ^{-1} extrapolates to zero at about −35 and −200 K for SA and SB, respectively. These negative signs indicate the antiferromagnetic character of the interactions among Fe moments, whose effective strength increases with the doping level. To further investigate the origin of the change of curvature in χ^{-1}, we fitted χ over the whole temperature range considering two temperature-dependent terms (see equation (4) below). In this way, we can separately consider contributions from magnetically isolated or correlated iron ions, following the model proposed in [15] to describe a similar behaviour observed in Co-and Mn-doped ZnO DMS. Thus, χ can be expressed as

$$\chi = \chi_0 + \frac{C_1}{T} + \frac{C_2}{T+\theta} \tag{4}$$

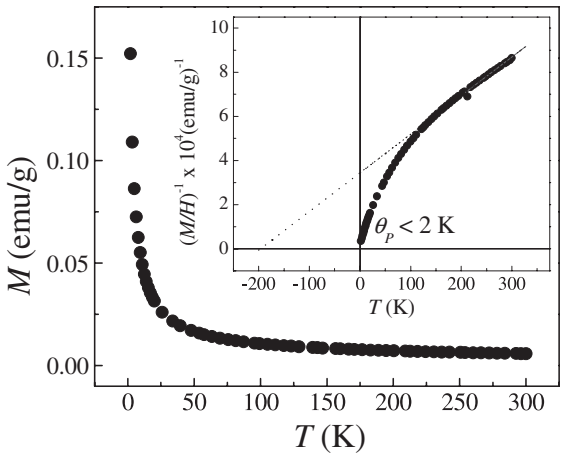

Figure 10. Thermal dependence of ZFC magnetization of sample SB measured by using a 1 kOe magnetic field. Inset: reciprocal magnetization versus temperature.

where χ_0 represents a weak temperature-independent contribution ($\sim 10^{-6}$ emu g^{-1} Oe^{-1}), C_1 and C_2 are the Curie constants for the magnetically isolated and interacting Fe ions, respectively, and θ is the Curie–Weiss temperature. Fitting results are shown in figure 9. Values of $\theta \sim 35$ and 192 K result for SA and SB, respectively. From these results and also assuming that the percentages of isolated Fe ions are those that remain paramagnetic at low temperature, we estimated the effective magnetic moments for isolated (μ_I) and interacting Fe ions (μ_c). For sample SB, $\mu_I \sim 5.82\ \mu_B$, near the contribution expected for free Fe^{3+} ions ($\mu_{Fe} \sim 5.92\ \mu_B$), while the reduced value for interacting Fe ions ($\mu_c \sim 4.56\ \mu_B$) would be an indication of short-ranged correlations between Fe^{3+} moments. However, for SA $\mu_c = 6.15\ \mu_B$, which is larger than $\mu_I = 5.88\ \mu_B$. This inconsistency was also found in Co and Mn substituted ZnO for small dopant concentration, its cause being uncertain [15].

We have also measured the thermal dependence of the dc magnetization of SB under zero field cooled (ZFC) and field cooled (FC) conditions (applied field $H_{FC} = 0.1$ T) (figure 10 shows the ZFC curve). These curves split slightly below 30 K (not shown here), and at 2 K the maximum ZFC–FC separation occurs (M_{FC}–$M_{ZFC} \sim 10^{-4}\ \mu_B$/Fe). The magnetization monotonically decreases with increasing temperature without showing any evidence of a long-range magnetic ordering below 300 K. Similarly to the inverse low-field susceptibility behaviour, the reciprocal magnetization, $M^{-1}(T)$, deviates from the high temperature linear trend at $\sim$120 K (inset figure 10). The paramagnetic temperature, θ_P, defined as the temperature at which $M^{-1}(T)$ extrapolates to zero [42], is $\theta_P < 2$ K. Besides, the extrapolation to zero of the high temperature linear region cuts the temperature axis at the negative temperature value of -197 K, in agreement with the results of χ shown in figure 9.

5. Discussion and conclusions

The local structural and hyperfine characterization of Fe-sites in Fe-doped anatase nanoparticles studied here shows that iron (III) mainly substitutes for titanium (IV) in the anatase structure. Indeed, x-ray absorption results revealed the particular electronic structure and local environment of Fe at Ti-sites in anatase TiO_2, and also showed that iron is in a 3+ oxidation state. Further, the doping causes an enlargement of cation–oxygen bond lengths around iron ions. Broad Fe^{3+} doublets in the room temperature Mössbauer spectra reflect paramagnetic Fe atoms having different environments. We fitted these spectra assuming two Fe^{3+} quadrupolar sites. Our calculations, assuming different structural scenarios, allow us to assign these two interactions to Fe(III) replacing Ti(IV) in anatase with oxygen vacancies close to the dopant. The site with the larger QS (site I) would correspond to oxygen vacancies placed at basal positions in an Fe octahedron, while site II to vacancies at apical positions. This confirms the assumption made by Balcells *et al* who applied bond valence rules and geometrical considerations to qualitatively interpret their Mössbauer results in Fe-doped rutile TiO_2 nanoparticles [18]. Finally, calculations including vacancies reproduce well the Fe–O_{NN} and Fe–Ti_{NN} distances obtained from EXAFS results. The presence of vacancies is also required to satisfy the charge neutrality of the samples.

Concerning the magnetic properties, our results give evidence of a paramagnetic state of iron in Fe-doped anatase at room temperature. Due to the low level of doping, the magnetic ions are expected to be far from each other so that any exchange or dipolar interaction between them is negligible. With increasing amount of iron, the emergence of magnetically coupled ions might be favoured. But a topological frustration is present and some Fe spins remain in a relaxation regime even at low temperatures. For $x = 5.4$ at.% (SB) a six-line spectrum is partially resolved at 4.2 K (within the Mössbauer window time of $\sim 10^{-8}$ s) due to the slowing down of the magnetic moment fluctuations. The freezing of the moments takes place within the 23–4.2 K interval. For $x = 2.8$ at.% (SA), the more diluted magnetic ions give rise to a weaker interaction that decreases the relaxation time and as a result the magnetic pattern collapses and time-dependent effects dominate the Mössbauer lineshape. Thus, the spin correlation that causes the deviation of the magnetization from its high temperature behaviour is not intense enough to establish a long-range order down to 2 K but a short-range spin order exists above θ_P. This is also reflected by the smaller effective magnetic moment of Fe in TiO_2 nanoparticles ($\sim$4.5–4.7 μ_B) with respect to free Fe^{3+} ions (5.9 μ_B). The lower magnetization value for SB (figure 8) is also an indication that more pronounced correlations are operative in this sample.

Therefore, from Mössbauer and magnetic analysis we differentiate: (i) isolated magnetic Fe ions that remain paramagnetic down to the lowest temperatures and (ii) magnetic interacting Fe ions, where an antiferromagnetic interaction establishes a short-range correlation. Indeed, even though the presence of substitutional iron plus oxygen vacancies around the magnetic impurities enhances the magnetic moment, it does not induce a ferromagnetic response in Fe-doped TiO_2 nanoparticles. Then, our results demonstrate that the presence of iron plus oxygen vacancies around the magnetic impurity is not enough to induce a ferromagnetic

response in Fe-doped TiO_2 nanoparticles. Thus, the reported ferromagnetism in similar Fe-doped TiO_2 systems should be explained in terms of other electronic defects provided than spurious magnetic phases can be completely ruled out.

Acknowledgments

We appreciate financial support by LNLS, Campinas-SP, Brazil (projects D04B-XAFS1-3492 and D04B-XAFS1-4148), CONICET, Argentina (PIP 6075 and PIP 6005), CSIC-CONICET (project 2004AR0070) and PICT 06-17492 (ANPCyT, Argentina). The dc-magnetic measurements were performed using the RN3M facilities. We thank M Fernández-García for kindly providing the material and D Sanchez and S G Marchetti for the low temperature Mössbauer spectra.

References

[1] Yu J C, Yu J, Ho W, Jiang Z and Zhang L 2002 *Chem. Mater.* **14** 3808
[2] Thompson T L and Yates J T Jr 2006 *Chem. Rev.* **106** 4428
[3] Belver C, Bellod R, Stewart S J, Requejo F G and Fernández-García M 2006 *Appl. Catal.* B **65** 309
[4] Adán C, Bahamonde A, Fernández-García M and Martínez-Arias A 2007 *Appl. Catal.* B **72** 11
[5] Li X, Yueb P-L and Kutal C 2003 *New J. Chem.* **27** 1264
[6] Choi W, Termin A and Hoffmann M R 1994 *J. Phys. Chem.* B **98** 13669
[7] Ikeda S, Sugiyama N, Murakami S, Kominami H, Kera Y, Noguchi H, Uosaki K, Torimoto T and Ohtan B 2005 *Phys. Chem. Chem. Phys.* **5** 778
[8] Cordishi D, Burriesci N, Dálba F, Petrera M, Polizzotti G and Schiavello M 1985 *J. Solid State Chem.* **56** 182
[9] Hirano M, Joji T, Inagaki M and Iwata H 2004 *J. Am. Ceram. Soc.* **87** 35
[10] Matsumoto Y, Murakami M, Shono T, Hasegawa T, Fukumura T, Kawasaki M, Ahmet P, Chikyow T, Koshihara S and Koinuma H 2001 *Science* **291** 854
[11] Park M S, Kwon S K and Min B H 2002 *Phys. Rev.* B **65** 161201(R)
[12] Kim J-Y, Park J-H, Park B-G, Noh H-J, Oh S-J, Yang J S, Kim D-H, Bu S D, Noh T-W, Lin H-J, Hsieh H-H and Chen C T 2003 *Phys. Rev. Lett.* **90** 017401
[13] Hong N H, Sakai J, Huong N T, Poirot N and Ruyter A 2005 *Phys. Rev.* B **72** 45336
[14] Griffin K A, Pakhomov A B, Wang C M, Heald S M and Krishnan K M 2005 *Phys. Rev. Lett.* **94** 157204
[15] Lawes G, Risbud A S, Ramirez A P and Seshadri R 2005 *Phys. Rev.* B **71** 045201
[16] Kim K J, Park Y R, Ahn G Y, Kim C S and Park J Y 2006 *J. Appl. Phys.* **99** 08M120
[17] Xiaoyan P, Dongmei J, Yan L and Xueming M 2006 *J. Magn. Magn. Mater.* **305** 388
[18] Balcells Ll, Frontera C, Sandiumenge F, Roig A, Martínez B, Kouam J and Monty C 2006 *Appl. Phys. Lett.* **89** 122501
[19] Lee H M and Kim C S 2007 *J. Magn. Magn. Mater.* **310** 2099
[20] Venkatesan M, Fitzgerald C B, Lunney J G and Coey J M D 2004 *Phys. Rev. Lett.* **93** 177206
[21] Zhu S, Li Y, Fan C, Zhang D, Liu W, Sun Z and Wei S 2005 *Physica* B **364** 199
[22] Yamaura K, Wang X H, Li J-G, Ishigaki T and Takayama-Muromachi E 2006 *Mater. Res. Bull.* **41** 2080
[23] Ravel B and Newville M 2005 *J. Synchrotron Radiat.* **12** 537
[24] Schatz G and Weidinger A 1996 *Nuclear Condensed Matter Physics: Nuclear Methods and Applications* (Chichester: Wiley)
[25] Mielczarek E V and Papaconstantopoulos D A 1978 *Phys. Rev.* B **17** 4223
Sánchez P, Friedt J M, Trautwein A and Reschke R 1979 *Phys. Rev.* B **19** 365
[26] Hill J and Howard C J 1987 *J. Appl. Crystallogr.* **20** 467
[27] Diebold U 2003 *Surf. Sci. Rep.* **48** 53
[28] Wei S H and Krakauer H 1985 *Phys. Rev. Lett.* **55** 1200
[29] Dufek P, Blaha P and Schwarz K 1995 *Phys. Rev. Lett.* **75** 3545
[30] Blaha P, Schwarz K, Madsen G K H, Kvaniscka D and Luitz J 2001 *WIEN2K, An Augmented Plane Wave+Local Orbitals Program for Calculating Crystal Properties* ed K Schwarz (Austria: Techn. Universität Wien)
[31] Perdew J P and Wang Y 1992 *Phys. Rev.* B **45** 13244
[32] Errico L A, Fabricius G and Rentería M 2003 *Phys. Rev.* B **67** 144104
[33] Blaha P, Schwarz K and Dederichs P H 1988 *Phys. Rev.* B **37** 2792
Schwarz K, Ambrosch-Draxl C and Blaha P 1990 *Phys. Rev.* B **42** 2051
[34] Brydson R, Sauer H, Engel W, Thomas J M, Zeitler E, Kosugi N and Kuroda H 1989 *J. Phys.: Condens. Matter* **1** 797
[35] Farges F, Brown G E Jr and Rehr J J 1997 *Phys. Rev.* B **56** 1809
[36] de Groot F 2001 *Chem. Rev.* **101** 1779
[37] Wilke M, Farges F, Petit P E, Brown G E Jr and Martin F 2001 *Am. Mineral.* **86** 714
[38] Newville M J 2001 *J. Synchrotron. Radiat.* **8** 322
Ravel B and Newville M J 2005 *J. Synchrotron. Radiat.* **12** 537
[39] Zhu S, Shi T, Liu W, Wei S, Xie Y, Fan C and Li Y 2007 *Physica* B **396** 177
[40] Borzi R A, Stewart S J, Punte G, Mercader R C, Zysler R, Vasquez-Mansilla M and Cabanillas E D 1999 *J. Magn. Magn. Mater.* **205** 234 and references therein
[41] Errico L A, Rentería M and Weissmann M 2005 *Phys. Rev.* B **72** 184425
[42] Cullity B D 1972 *Introduction to Magnetic Materials* (Reading, MA: Addison-Wesley)